

An FFT-accelerated PML-BIE Solver for Three-Dimensional Acoustic Wave Scattering in Layered Media

Hangya Wang¹ and Wangtao Lu¹

December 17, 2024

Abstract

This paper is concerned with three-dimensional acoustic wave scattering in two-layer media, where the two homogeneous layers are separated by a locally perturbed plane featuring an axially symmetric perturbation. A fast novel boundary integral equation (BIE) method is proposed to solve the scattering problem within a cylindrical perfectly matched layer (PML) truncation. We use PML-transformed Green's functions to derive BIEs in terms of single- and double-layer potentials for the wave field and its normal derivative on the boundary of each truncated homogeneous region. These BIEs, combined with interface and PML boundary conditions, form a complete system that accurately approximates the scattering problem. An FFT-based approach is introduced to efficiently and accurately discretize the surface integral operators in the BIEs, where a new kernel splitting technique is developed to resolve instabilities arising from the complex arguments in Green's functions. Numerical experiments demonstrate the efficiency and accuracy of the proposed method, as well as the exponential decay of truncation errors introduced by the PML.

1 Introduction

Wave scattering phenomena in layered media play a crucial role in various domains of physics and engineering, including acoustics, electromagnetics, and elastodynamics. These phenomena are fundamental to understanding wave propagation mechanisms over complex surfaces and near-field optical interactions, with critical applications ranging from geophysical exploration to nano-optics[10]. Recently, there has been increasing interest in axisymmetric structures[16, 26]. Despite the significance of these problems, various challenges limit the availability of accurate and efficient numerical solutions. Traditional numerical methods, such as the Finite Element Method (FEM) [24], while widely implemented, become too expensive when the scatterer size significantly exceeds the wavelength. In contrast, the BIE method [12] provides an effective alternative for various scattering scenarios [4, 6, 34]. This approach has two main advantages: it reduces the problem dimension by one and inherently satisfies the outgoing radiation condition. For large-scale problems, the BIE method outperforms classical discretization methods, enabling faster and higher-order algorithms.

BIE solvers for layered medium scattering problems can be broadly categorized into two principal approaches. The first approach uses the background Green's functions of the layered medium [30, 27, 28], with integral equations formulated at local interfaces or boundaries. These Green's functions are defined only on the bounded region of

¹School of Mathematical Sciences, Zhejiang University, Hangzhou 310027, China. Email: wangtaolu@zju.edu.cn, wangmy123@zju.edu.cn.

the scattering surface, thereby eliminating the need for additional truncation. However, this approach presents a significant computational challenge due to the need to evaluate complex Sommerfeld integrals arising from the layered-medium Green’s function and its derivatives. A comprehensive computational cost analysis for evaluating the Sommerfeld integrals is available in [7]. The second approach employs free-space Green’s functions and requires the formulation of integral equations on unbounded interfaces between different background medium layers. While this approach avoids intricate Sommerfeld integrals, special treatments are required to truncate the unbounded surface. These treatments include the approximate truncation method [22, 29], the taper function method [23, 31, 35], and the windowed function method [5, 1, 6]. The windowed Green function method [5] attains superior performance through a correction and ensures uniformly fast convergence across all incident angles as the window size increases.

Recently, [20] proposed a BIE method based on PMLs for two-dimensional (2D) scattering problems in layered media. Similar to BIE methods based on the free-space Green’s function, this approach avoids evaluating expensive Sommerfeld integrals by formulating integral equations along the interfaces of the background layered medium. This method employs the PML-transformed free-space Green’s function to attenuate outgoing waves, enabling direct truncation of the unbounded scattering domain and leading to solutions that converge exponentially [9]. So far, this approach has been successfully extended to more complex structures, including step-scattering surfaces [19], anisotropic media [14], localized regenerative periodic structures [33]. and 2D layered media with local smooth defects. Notably, [21] extends this approach to three dimensions and develops efficient treatment for the hyper-singular boundary integral operators.

In this paper, we develop a novel FFT-accelerated PML-BIE method for 3D acoustic scattering problems in axially symmetric, piecewise homogeneous media. The computational domain comprises two homogeneous regions separated by a flat interface containing a finite, axially symmetric perturbation. Employing PML technology efficiently handles the unbounded domain. Due to the axisymmetry, our method has significant advantages in the following aspects. Our approach is based on a direct boundary integral formulation derived from Green’s representation theorem, which avoids the discretization of hyper-singular boundary integral operators. With axisymmetry, we apply Fourier transformation to reduce the surface integral equations into a series of decoupled curve integral equations [32]. The decoupling enables the use of the FFT to enhance computational efficiency significantly. To accurately evaluate both regular and singular integrals, we employ high-order quadrature rules developed by Alpert[2]. To address instability issues and obtain accurate PML-transformed modal Green’s functions, we propose a modified kernel-splitting technique based on function substitutions and numerical techniques. A carefully designed graded mesh scheme [12] that effectively captures solution behavior near singularities is employed to solve the geometric singularity. Numerical experiments demonstrate that the PML truncation of unbounded interfaces is effective, yielding high-accuracy results when appropriate PML parameters are selected.

The rest of this paper is organized as follows: Section 2 presents the formulation of scattering problems in piecewise constant penetrable media. Section 3 introduces boundary integral equations for the truncated PML problem and applies Fourier transformation to these equations. Section 4 details the numerical discretization scheme for the integral equations and several significant numerical techniques. Finally, Section 5 demonstrates the performance of our method through numerical experiments.

2 Problem formulation

As illustrated in Figure 1, the layered medium consists of two homogeneous domains, denoted as Ω_1 and Ω_2 . The interface Γ separating Ω_1 and Ω_2 consists of an infinite flat surface $z = 0$ and an axisymmetric perturbation surface. In what follows, we assume that the surface Γ is piecewise smooth and contains a finite number of corners/edges.

Let u^{inc} represent a time-harmonic incident wave field with time-dependence $e^{-i\omega t}$. The total wave field after scattering is denoted by u^{tot} . In the standard Cartesian coordinate system, the governing 3D Helmholtz equation for u^{tot} is

$$\Delta u^{tot} + \frac{\omega^2}{c^2(\mathbf{r})} u^{tot} = 0, \quad \text{in } \mathbb{R}^3, \quad \text{eq:helm} \quad (1)$$

where $\mathbf{r} = (x, y, z)$, ω denotes the angular frequency and $\Delta = \partial_x^2 + \partial_y^2 + \partial_z^2$ represents the 3D Laplacian operator. Here, $c(\mathbf{r})$ represents the speed of sound in the layered media, which is given by

$$c(\mathbf{r}) = c_j, \quad \text{in } \Omega_j, \quad j = 1, 2.$$

For simplicity, the density is assumed to be constant throughout the entire space. Let $\omega_j = \omega/c_j$, with $c_1 = 1$. Across the interface Γ , the total wave field u^{tot} satisfies the continuity condition

$$[u^{tot}] = 0, \quad \text{and} \quad \left[\frac{\partial u^{tot}}{\partial \nu} \right] = 0, \quad \text{eqbdc} \quad (2)$$

where $[\cdot]$ denotes the jump of the quantity, and ν is the unit outer normal vector on Γ towards Ω_2 . Since the total field u^{tot} does not satisfy the outgoing radiation condition, we express it as the sum of a reference wave field $u^{tot,0}$, defined as follows, and a scattered wave field $u^s = u^{tot} - u^{tot,0}$.

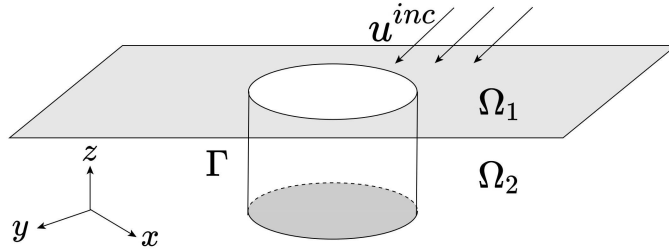


Figure 1. Profile of a 3D layered medium.

fg1

In this paper, we consider two types of incident waves, a plane wave and a spherical wave excited by a point source. For plane wave incidence, we assume the incident wave is given by

$$u^{inc} = e^{i\omega_1(-x \sin \phi^{inc} \cos \theta^{inc} - y \sin \phi^{inc} \sin \theta^{inc} - z \cos \phi^{inc})}, \quad \text{eqpw1} \quad (3)$$

where the polar angle $\phi^{inc} \in [0, \pi/2)$ and the azimuthal angle $\theta^{inc} \in [0, 2\pi)$. Due to the axial symmetry of the layered structure, we set $\theta^{inc} = 0$. This simplifies equation (3) to

$$u^{inc} = e^{i\omega_1(-x \sin \phi^{inc} - z \cos \phi^{inc})}. \quad \text{eqpw} \quad (4)$$

The reference wave field $u^{tot,0}$ is defined as the solution of the incident wave u^{inc} scattered by a flat interface at $z = 0$. The explicit expression for $u^{tot,0}$ is given by

$$u^{tot,0} = \begin{cases} e^{i\omega_1(-x \sin \phi^{inc} - z \cos \phi^{inc})} + R e^{i\omega_1(-x \sin \phi^{inc} + z \cos \phi^{inc})}, & \text{in } \Omega_1, \\ (R + 1) e^{-i\omega_1 x \sin \phi^{inc} - i k^* z}, & \text{in } \Omega_2, \end{cases} \quad (5)$$

where

$$R = \frac{2}{1 + \frac{k^*}{\omega_1 \cos \phi^{inc}}} - 1. \quad (6)$$

Here, k^* is defined as

$$k^* = \begin{cases} \sqrt{\omega_2^2 - \omega_1^2 \sin^2 \phi^{inc}}, & \omega_2 > |\omega_1 \sin \phi^{inc}|, \\ \mathbf{i} \sqrt{\omega_1^2 \sin^2 \phi^{inc} - \omega_2^2}, & \omega_2 \leq |\omega_1 \sin \phi^{inc}|. \end{cases} \quad (7)$$

For spherical wave incidence, equation (1) is modified to

$$\Delta u^{tot} + \omega_j^2 u^{tot} = -\delta(\mathbf{r}, \mathbf{r}^*), \quad \text{in } \Omega_j, \quad j = 1, 2, \quad \text{eq:helm1} \quad (8)$$

where $\mathbf{r}^* = (x^*, y^*, z^*)$ represents the coordinates of the source point. The incident wave is expressed as

$$u^{inc} = \frac{e^{\mathbf{i}\omega_1|\mathbf{r}-\mathbf{r}^*|}}{4\pi|\mathbf{r}-\mathbf{r}^*|}. \quad (9)$$

For $\mathbf{r}^* \in \Omega_1$, the reference wave field $u^{tot,0}$ is given by

$$u^{tot,0} = \begin{cases} u^{inc}, & \text{in } \Omega_1, \\ 0, & \text{in } \Omega_2. \end{cases} \quad (10)$$

Based on equation (1) and the definition of $u^{tot,0}$, the scattered field u^s satisfies the Helmholtz equation

$$\Delta u^s + \omega_j^2 u^s = 0, \quad \text{in } \Omega_j, \quad j = 1, 2. \quad (11)$$

At infinity, the scattered field u^s satisfies the following half-space Sommerfeld radiation condition

$$\lim_{|\mathbf{r}| \rightarrow \infty} |\mathbf{r}| (\partial_{|\mathbf{r}|} - \mathbf{i}\omega_j) u^s = 0, \quad \text{in } \Omega_j, \quad j = 1, 2, \quad (12)$$

where $|\cdot|$ denote the Euclidean norm; see the equivalent upward propagating radiation condition [3, 8] for more details. Instead of computing u^{tot} directly, we focus on computing the scattered field u^s , which satisfies the following boundary conditions on the interface Γ :

$$\begin{aligned} u^{s,1}|_{\Gamma} - u^{s,1}|_{\Gamma} &= -[u^{tot,0}], & \text{eqs1} & (13) \\ \frac{\partial u^{s,1}}{\partial \nu}|_{\Gamma} - \frac{\partial u^{s,2}}{\partial \nu}|_{\Gamma} &= -\left[\frac{\partial u^{tot,0}}{\partial \nu}\right], & \text{eqs2} & (14) \end{aligned}$$

where $u^{s,j}$ denotes u^s in Ω_j , for $j = 1, 2$. In the following section, we will introduce a PML-based BIE formulation for solving the scattering problems.

3 The PML truncation and boundary integral equations.

This section introduces the PML truncation and the boundary integral equations associated with the truncated PML problems. Without loss of generality, we restrict our analysis to the upper homogeneous domain Ω_1 . Henceforth, we denote $u^{s,1}$ and ω_1 simply as u^s and ω , respectively.

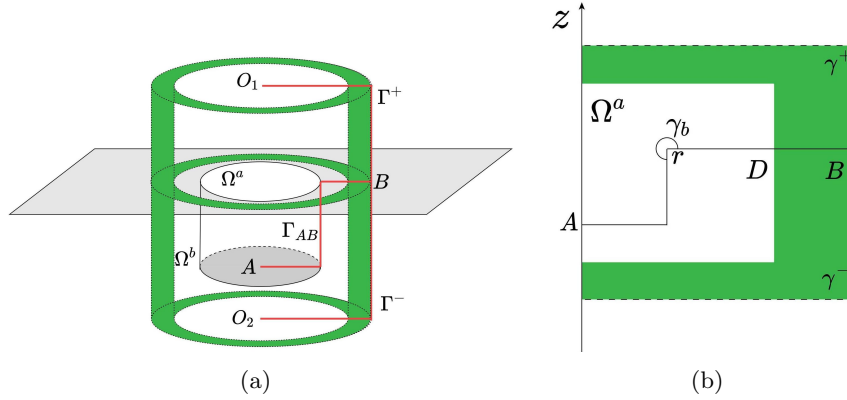


Figure 2. (a) The 3D illustration of the PML truncation. (b) The 2D cross-section of the PML truncation. fg2

3.1 Boundary integral equations for the PML problem

As illustrated in Figure 2(a), a cylindrical PML, represented by the green region, is employed to enclose the perturbation and truncate the domain \mathbb{R}^3 . Let Γ_{AB} , Γ^+ and Γ^- denote the surfaces generated by rotating the red polylines connecting points A to B , B to O_1 , and B to O_2 , respectively. The cylindrical domain consists of two bounded domains Ω^a and Ω^b with boundaries $\Gamma^a = \Gamma^+ \cup \Gamma_{AB}$ and $\Gamma^b = \Gamma^- \cup \Gamma_{AB}$, respectively. Following [11], we introduce a complex coordinate stretching $\tilde{\mathbf{r}}(\mathbf{r}) = (\tilde{\rho} \cos \theta, \tilde{\rho} \sin \theta, \tilde{z})$, which is defined as

$$\begin{aligned} \tilde{\rho}(\rho) &= \rho + \mathbf{i} \int_0^\rho \sigma_1(t) dt, & \text{eqrho} \tag{15} \\ \tilde{z}(z) &= z + \mathbf{i} \int_0^z \sigma_2(t) dt, & \text{eqzt} \tag{16} \end{aligned}$$

where $\sigma_l(t) = \sigma_l(-t)$, $\sigma_l(t) = 0$ for $|t| \leq a_l$ and $\sigma_l(t) > 0$ for $|t| > a_l$, for $l = 1, 2$. In principle, σ_l can be any positive function in the PML. For definiteness, taking σ_1 as an example, it is defined as

$$\sigma_1(\rho) = \begin{cases} \frac{2Sf_1^p}{f_1^p + f_2^p}, & a_1 \leq \rho \leq a_1 + T, \\ S, & \rho > a_1 + T, \\ 0, & a_1 < \rho < a_1, \\ \sigma_1(-\rho), & \rho \leq -a_1, \end{cases} \quad \text{eqsgm1} \tag{17}$$

where p is a positive integer,

$$f_1 = \left(\frac{1}{2} - \frac{1}{p} \right) \bar{\rho}^3 + \frac{\bar{\rho}}{p} + \frac{1}{2}, \quad f_2 = 1 - f_1, \quad \bar{\rho} = \frac{\rho - (a_1 + T)}{T}. \quad (18)$$

The function $\sigma_1(\rho)$ maps the interval $[a_1, a_1 + T]$ to $[0, S]$, where T represents the PML thickness and S determines the magnitude of $\sigma_1(\rho)$. Additionally, the derivatives of the function σ_1 vanish at $\rho = \pm a_1$ up to order $p - 1$. A similar definition applies to σ_2 .

According to Lemma 2.3 in [18], the scattered field $u^s(\mathbf{r})$ can be analytically continued into the $\tilde{\Omega}^a = \{\tilde{\mathbf{r}}(\mathbf{r}) | \mathbf{r} \in \Omega^a\}$. Within this domain, $u^s(\tilde{\mathbf{r}})$ satisfies the equation

$$\tilde{\Delta} u^s(\tilde{\mathbf{r}}) + \omega^2 u^s(\tilde{\mathbf{r}}) = 0, \quad \text{in } \tilde{\Omega}^a, \quad \text{eqht} \tag{19}$$

where $\tilde{\Delta} = \frac{\partial^2}{\partial \tilde{\rho}^2} + \frac{1}{\tilde{\rho}} \frac{\partial}{\partial \tilde{\rho}} + \frac{1}{\tilde{\rho}^2} \frac{\partial^2}{\partial \theta^2} + \frac{\partial^2}{\partial \tilde{z}^2}$. Applying Green's representation theorem, the solution of (19) can be expressed as

$$u^s(\tilde{\mathbf{r}}) = \int_{\Gamma^a} \{G(\tilde{\mathbf{r}}, \mathbf{r}') \partial_\nu u^s(\mathbf{r}') - \partial_\nu G(\tilde{\mathbf{r}}, \mathbf{r}') u^s(\mathbf{r}')\} d\mathbf{r}'. \quad (20)$$

Using the notation $\tilde{u}^s(\mathbf{r}) = u^s(\tilde{\mathbf{r}})$ and chain rule, equation (19) can be reorganized as

$$\nabla \cdot (\mathbf{A} \nabla \tilde{u}^s) + \omega^2 J \tilde{u}^s = 0, \quad \text{on } \Omega^a, \quad \text{eqht2} \quad (21)$$

where $\alpha_\rho(\rho) = 1 + i\sigma_1(\rho)$, $\alpha_z(z) = 1 + i\sigma_2(z)$, $\mathbf{A} = \text{diag}(\frac{\tilde{\rho}\alpha_z}{\rho\alpha_\rho}, \frac{\rho}{\tilde{\rho}}\alpha_\rho\alpha_z, \frac{\tilde{\rho}\alpha_\rho}{\rho\alpha_z})$, $J = \frac{\tilde{\rho}}{\rho}\alpha_\rho\alpha_z$. According to the Lemma 2.8 in [18], the fundamental solution of (21) is

$$\tilde{G}(\mathbf{r}, \mathbf{r}') = G(\tilde{\mathbf{r}}, \tilde{\mathbf{r}}') = \frac{e^{i\omega|\tilde{\mathbf{r}}-\tilde{\mathbf{r}}'|}}{4\pi|\tilde{\mathbf{r}}-\tilde{\mathbf{r}}'|}, \quad \tilde{\mathbf{r}} \neq \tilde{\mathbf{r}}', \quad (22)$$

where the complexified distance function is defined as

$$|\tilde{\mathbf{r}} - \tilde{\mathbf{r}}'| = \sqrt{\tilde{\rho}^2 + \tilde{\rho}'^2 - 2\tilde{\rho}\tilde{\rho}' \cos(\theta - \theta') + (\tilde{z} - \tilde{z}')^2}. \quad (23)$$

Throughout this paper, for the function \sqrt{z} , we choose the negative real axis as the branch cut, ensuring that the argument $\arg \sqrt{z}$ lies within $(-\pi/2, \pi/2]$. Using the results in [20], we have the following integral representation

$$\tilde{u}^s(\mathbf{r}) = \int_{\Gamma^a} \left\{ \frac{\partial \tilde{u}^s}{\partial \nu_c}(\mathbf{r}') \tilde{G}(\mathbf{r}, \mathbf{r}') - \tilde{u}^s(\mathbf{r}') \frac{\partial \tilde{G}(\mathbf{r}, \mathbf{r}')}{\partial \nu_c(\mathbf{r}')} \right\} dS(\mathbf{r}'), \quad \mathbf{r} \in \Omega^a, \quad \text{eqg1t} \quad (24)$$

where

$$\nu_c = \mathbf{A}^T \nu = \left(\nu_\rho \cos \theta \frac{\tilde{\rho}\alpha_z}{\rho\alpha_\rho}, \nu_\rho \sin \theta \frac{\tilde{\rho}\alpha_z}{\rho\alpha_\rho}, \nu_z \frac{\tilde{\rho}\alpha_\rho}{\rho\alpha_z} \right), \quad (25)$$

and $\frac{\partial}{\partial \nu_c} = \nu_c \cdot \nabla$. For simplicity, $\nu_\rho \frac{\tilde{\rho}\alpha_z}{\rho\alpha_\rho}$ and $\nu_z \frac{\tilde{\rho}\alpha_\rho}{\rho\alpha_z}$ are denoted by $\nu_{c,\rho}$ and $\nu_{c,z}$, respectively. As \mathbf{r} approaches the boundary Γ^a , equation (24) becomes

$$\left(\tilde{\mathcal{K}} - \tilde{\mathcal{K}}^0 1 \right) \tilde{u}^s = \tilde{\mathcal{S}} \partial_{\nu_c} \tilde{u}^s, \quad \text{on } \Gamma^a. \quad \text{eq4} \quad (26)$$

where

$$(\tilde{\mathcal{S}}\varphi)(\mathbf{r}) = 2 \int_{\Gamma^a} \tilde{G}(\mathbf{r}, \mathbf{r}') \varphi(\mathbf{r}') dS(\mathbf{r}'), \quad \mathbf{r} \in \Gamma^a, \quad \text{eq:St} \quad (27)$$

$$(\tilde{\mathcal{K}}\varphi)(\mathbf{r}) = 2 \rlap{-}\int_{\Gamma^a} \frac{\partial \tilde{G}(\mathbf{r}, \mathbf{r}')}{\partial \nu_c(\mathbf{r}')} \varphi(\mathbf{r}') dS(\mathbf{r}'), \quad \mathbf{r} \in \Gamma^a, \quad \text{eq:Kt} \quad (28)$$

$$(\tilde{\mathcal{K}}^0 \varphi)(\mathbf{r}) = 2 \rlap{-}\int_{\Gamma^a} \frac{\partial \tilde{G}_0(\mathbf{r}, \mathbf{r}')}{\partial \nu_c(\mathbf{r}')} \varphi(\mathbf{r}') dS(\mathbf{r}'), \quad \mathbf{r} \in \Gamma^a. \quad \text{eq:K0t} \quad (29)$$

Here, $\rlap{-}\int$ denotes the Cauchy principal value integral and $\tilde{G}_0(\mathbf{r}, \mathbf{r}') = \frac{1}{4\pi|\tilde{\mathbf{r}}-\tilde{\mathbf{r}}'|}$ represents the Green's function of the complexified Laplace equation

$$\nabla \cdot (\mathbf{A} \nabla \tilde{u}_{n,0}^s(\mathbf{r})) = 0. \quad (30)$$

Finally, $\tilde{\mathcal{K}}^0 1(\mathbf{r})$ is defined as

$$\tilde{\mathcal{K}}^0 1(\mathbf{r}) = 2 \rlap{-}\int_{\partial\Omega^a} \frac{\partial \tilde{G}_0(\mathbf{r}, \mathbf{r}')}{\partial \nu_c(\mathbf{r}')} dS(\mathbf{r}'), \quad \mathbf{r} \in \Gamma^a. \quad \text{eqk01_2t} \quad (31)$$

3.2 Truncation of boundary integral equations onto Γ_{AB}

The PML is an artificial absorbing region designed to effectively absorb outgoing waves, ensuring that the scattered field u^s and its normal derivative $\partial_\nu u^s$ decay rapidly within the PML before reaching its outer boundary. Due to the absorption properties of the PML, it is appropriate to approximate $\tilde{u}^s \approx 0$ and $\partial_{\nu_c} \tilde{u}^s \approx 0$ on Γ^+ . Equation (26) can be truncated as

$$(\tilde{\mathcal{K}}_{AB} \tilde{u}^s - \tilde{\mathcal{K}}^0 1) \tilde{u}^s = \tilde{\mathcal{S}}_{AB} \partial_{\nu_c} \tilde{u}^s, \quad \text{on } \Gamma_{AB}, \quad \text{eqk0ab} \tag{32}$$

where $\tilde{\mathcal{K}}_{AB}$ and $\tilde{\mathcal{S}}_{AB}$ are the same as $\tilde{\mathcal{K}}$ and $\tilde{\mathcal{S}}$, respectively, but with the integral domain replaced by Γ_{AB} . However, the truncation of $\tilde{\mathcal{K}}^0 1$ onto Γ_{AB} is not straightforward.

To analyze the operator $\tilde{\mathcal{K}}^0 1$, we first consider the operator

$$\mathcal{K}^0 1(\mathbf{r}) = 2 \int_{\partial\Omega^a} \frac{\partial G_0(\mathbf{r}, \mathbf{r}')}{\partial \nu(\mathbf{r}')} dS(\mathbf{r}'), \quad \mathbf{r} \in \Gamma^a, \quad \text{eqk01_2} \tag{33}$$

which is defined as in (31) but with $\tilde{G}_0(\mathbf{r}, \mathbf{r}')$ replaced by $G_0(\mathbf{r}, \mathbf{r}') = \frac{1}{4\pi|\mathbf{r}-\mathbf{r}'|}$. For the operator $\mathcal{K}^0 1$, we have the following Lemma.

lem:K01

Lemma 3.1. *For any $\mathbf{r} \in \Gamma^a$, we have*

$$\mathcal{K}^0 1 = 1 - \cos \phi_0, \quad \text{eqk0_1} \tag{34}$$

where ϕ_0 is half the angle of the curve γ_b , see γ_b in Figure 2(b).

Proof. Using Green's identity, equation (33) can be rewritten as

$$\begin{aligned} \mathcal{K}^0 1(\mathbf{r}) &= \lim_{r_c \rightarrow 0^+} 2 \int_{\partial B(\mathbf{r}, r_c) \cap \overline{\Omega^a}} \partial_\nu G_0(\mathbf{r}, \mathbf{r}') dS(\mathbf{r}') && \text{eqk01t} \tag{35} \\ &= \lim_{r_c \rightarrow 0^+} \int_{\partial B(\mathbf{r}, r_c) \cap \overline{\Omega^a}} \frac{\boldsymbol{\nu}(\mathbf{r}') \cdot (\mathbf{r} - \mathbf{r}')}{2\pi |\mathbf{r} - \mathbf{r}'|^3} \rho' dS(\mathbf{r}'), && \text{eqk03} \tag{36} \end{aligned}$$

where $\partial B(\mathbf{r}, r_c)$ is a sphere centered at \mathbf{r} with radius r_c , and the unit normal vector $\boldsymbol{\nu}$ points toward Ω^b .

Next, we parameterize $\partial B(x, r_c)$ by

$$\mathbf{r}' = \mathbf{r} + r_c(\sin \phi \cos \theta, \sin \phi \sin \theta, \cos \phi), \quad \text{eqk04} \tag{37}$$

for $\theta \in [-\pi, \pi]$ and $\phi \in [0, \pi]$. Let γ_b denotes the projection of $\partial B(\mathbf{r}, r_c) \cap \overline{\Omega^a}$ on ρ - z half-plane. With coordinate axis rotation and the parameterisation (37), equation (36) becomes

$$\mathcal{K}^0 1(\mathbf{r}) = \frac{1}{2\pi} \int_{\gamma_b} \int_{-\pi}^{\pi} \frac{r_c}{r_c^3} \rho_s^2 \sin \phi d\theta d\phi \tag{38}$$

$$= \int_0^{\phi_0} \sin \phi d\phi \tag{39}$$

$$= 1 - \cos \phi_0, \tag{40}$$

where ρ_s denotes the radial distance in the spherical coordinate system, and (34) follows. \square

For $\tilde{\mathcal{K}}^0 1$, we have the following Lemma.

Lemma 3.2. For any $\mathbf{r} \in \Gamma^a$, we have

$$\tilde{\mathcal{K}}^0 \mathbf{1} = 1 - \cos \phi_0.$$

eqk0_1t
(41)

where ϕ_0 is half the angle of the curve γ_b .

Proof. Using Green's identity, we can easily see that

$$\tilde{\mathcal{K}}^0 \mathbf{1}(\mathbf{r}) = \lim_{r_c \rightarrow 0^+} \int_{\partial B(\mathbf{r}, r_c) \cap \bar{\Omega}^a} \frac{\boldsymbol{\nu}_c(\tilde{\mathbf{r}}') \cdot (\tilde{\mathbf{r}} - \tilde{\mathbf{r}}')}{2\pi |\tilde{\mathbf{r}} - \tilde{\mathbf{r}}'|^3} \rho' ds(\mathbf{r}') \quad \text{eqk03t, (42)}$$

where $\partial B(\mathbf{r}, r_c)$ is a sphere centered at \mathbf{r} with radius r_c . Let the points \mathbf{r} and \mathbf{r}' be denoted by (r_1, r_2, r_3) and (r'_1, r'_2, r'_3) , respectively. Similarly, $\tilde{\mathbf{r}}$ and $\tilde{\mathbf{r}}'$ are denoted by $(\tilde{r}_1, \tilde{r}_2, \tilde{r}_3)$ and $(\tilde{r}'_1, \tilde{r}'_2, \tilde{r}'_3)$, respectively.

By (15), (16) and (37), we have

$$\tilde{r}'_1 - \tilde{r}_1 = \int_{r_1}^{r'_1} \alpha_\rho(\sqrt{s^2 + r_2^2}) ds \quad (43)$$

$$= \int_{r_1}^{r_1 + r_c \sin \phi \cos \theta} \alpha_\rho(\sqrt{s^2 + r_2^2}) ds \quad (44)$$

$$= \alpha_\rho \left(\sqrt{r_1^2 + r_2^2} \right) r_c \sin \phi \cos \theta + O(r_c^2). \quad (45)$$

Similarly,

$$\tilde{r}'_2 - \tilde{r}_2 = \alpha_\rho \left(\sqrt{r_2^2 + r_1^2} \right) r_c \sin \phi \sin \theta + O(r_c^2) \quad (46)$$

$$\tilde{r}'_3 - \tilde{r}_3 = \alpha_z(r_3) r_c \cos \phi + O(r_c^2). \quad (47)$$

With coordinate axis rotation, as r_c approaches 0, equation (42) becomes

$$\tilde{\mathcal{K}}^0 \mathbf{1}(\tilde{\mathbf{r}}) = \frac{1}{2\pi} \int_{\gamma_b} \int_{-\pi}^{\pi} \frac{\alpha_\rho^2 \sin^2(\phi) + \alpha_z^2 \cos^2(\phi)}{\alpha_\rho^2 \sin^2(\phi) + \alpha_z^2 \cos^2(\phi)} \frac{\rho_s^2}{r_c^2} \sin \phi d\theta d\phi \quad (48)$$

$$= \int_0^{\phi_0} \sin \phi d\phi \quad (49)$$

$$= 1 - \cos \phi_0, \quad (50)$$

and (41) follows. \square

Comparing (34) and (41) gives

$$\begin{aligned} \tilde{\mathcal{K}}^0 \mathbf{1}(\mathbf{r}) &= \mathcal{K}^0 \mathbf{1}(\mathbf{r}) \\ &= \mathcal{K}_{AB}^0 \mathbf{1}(\mathbf{r}) + \mathcal{K}_+^0 \mathbf{1}(\mathbf{r}), \end{aligned} \quad \begin{array}{l} (51) \\ \text{k01bc} \\ (52) \end{array}$$

where the definitions of \mathcal{K}_{AB}^0 and \mathcal{K}_+^0 are the same as \mathcal{K}^0 but with the integral domain replaced by γ_{AB} and γ^+ , respectively.

To illustrate that the operator $\mathcal{K}_+^0 \mathbf{1}(\mathbf{r})$ can be computed concisely, we give an auxiliary geometric configuration, as depicted in Figure 3. Let Γ_{OB} denote the circle centered at origin O with radius l_{OB} , where l_{OB} is the length of OB . Let $\Gamma_{\mathbf{r}}$ denote the conical surface with Γ_{OB} as the base and \mathbf{r} as the vertex, where the point $\mathbf{r} = (\rho \cos \theta, \rho \sin \theta, z)$. Let ∂B_ϵ represents the sphere centered at \mathbf{r} with radius ϵ . The intersection of the surface ∂B_ϵ and the conical surface $\Gamma_{\mathbf{r}}$ forms the surface Γ_ϵ . In the following lemma, we provide a precise representation for $\mathcal{K}_+^0 \mathbf{1}(\mathbf{r})$.

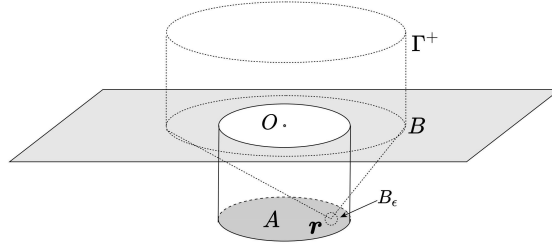


Figure 3. Geometric configuration for computing $\mathcal{K}_+^0 1(\mathbf{r})$

fg8

Lemma 3.3. For any \mathbf{r} on Γ_{AB} , we have

$$\mathcal{K}_+^0 1(\mathbf{r}) = \frac{1}{2\pi\epsilon^2} \int_{\Gamma_\epsilon} \rho_s^2 \sin \phi dS(\mathbf{r}'), \quad \text{k01bc1} \quad (53)$$

where ρ_s denotes the radial distance in the spherical coordinate system.

Proof. According to the definition of $\mathcal{K}_+^0 1$, we have

$$\mathcal{K}_+^0 1(\mathbf{r}) = \frac{1}{2\pi} \int_{\Gamma_+} \frac{\boldsymbol{\nu}(\mathbf{r}') \cdot (\mathbf{r} - \mathbf{r}')}{|\mathbf{r} - \mathbf{r}'|^3} \rho' dS(\mathbf{r}'). \quad \text{eqbdc1} \quad (54)$$

Applying the divergence theorem yields

$$\begin{aligned} \int_{\Gamma_+} \frac{\boldsymbol{\nu}(\mathbf{r}') \cdot (\mathbf{r} - \mathbf{r}')}{|\mathbf{r} - \mathbf{r}'|^3} \rho' dS(\mathbf{r}') + \int_{\Gamma_r} \frac{\boldsymbol{\nu}(\mathbf{r}') \cdot (\mathbf{r} - \mathbf{r}')}{|\mathbf{r} - \mathbf{r}'|^3} \rho' dS(\mathbf{r}') \\ + \int_{\Gamma_\epsilon} \frac{\boldsymbol{\nu}(\mathbf{r}') \cdot (\mathbf{r} - \mathbf{r}')}{|\mathbf{r} - \mathbf{r}'|^3} \rho' dS(\mathbf{r}') = 0. \end{aligned} \quad (55)$$

For $\mathbf{r}' \in \Gamma_r$, vectors $\boldsymbol{\nu}(\mathbf{r}')$ and $\mathbf{r} - \mathbf{r}'$ are orthogonal, leading to

$$\int_{\Gamma_r} \frac{\boldsymbol{\nu}(\mathbf{r}') \cdot (\mathbf{r} - \mathbf{r}')}{|\mathbf{r} - \mathbf{r}'|^3} \rho' dS(\mathbf{r}') = 0. \quad \text{eqbdc2} \quad (56)$$

Combining equations (54) and (56) yields

$$\mathcal{K}_+^0 1(\mathbf{r}) = \frac{-1}{2\pi} \int_{\Gamma_\epsilon} \frac{\boldsymbol{\nu}(\mathbf{r}') \cdot (\mathbf{r} - \mathbf{r}')}{|\mathbf{r} - \mathbf{r}'|^3} \rho' dS(\mathbf{r}'). \quad \text{ek0j} \quad (57)$$

The surface Γ_ϵ is parameterized as

$$\mathbf{r}' = \mathbf{r} + \epsilon(\sin \phi \cos \theta, \sin \phi \sin \theta, \cos \phi), \quad (58)$$

so that $\boldsymbol{\nu}(\mathbf{r}') = (\sin \phi \cos \theta, \sin \phi \sin \theta, \cos \phi)$. Thus, equation (57) becomes

$$\mathcal{K}_+^0 1(\mathbf{r}) = \frac{-1}{2\pi} \int_{\Gamma_\epsilon} \frac{\boldsymbol{\nu}(\mathbf{r}') \cdot (\mathbf{r} - \mathbf{r}')}{|\mathbf{r} - \mathbf{r}'|^3} \rho_s^2 \sin \phi dS(\mathbf{r}') \quad (59)$$

$$= \frac{1}{2\pi\epsilon^2} \int_{\Gamma_\epsilon} \rho_s^2 \sin \phi dS(\mathbf{r}'), \quad (60)$$

and this completes the proof. \square

Remark 3.1. The integral $\int_{\Gamma_\epsilon} \rho_s^2 \sin \phi dS(\mathbf{r}')$ and $4\pi\epsilon^2$ are the areas of surfaces Γ_ϵ and ∂B_ϵ , respectively. The areas of surface Γ_ϵ can be computed numerically via the Alpert quadrature rule. Hence, the computation of $\mathcal{K}_+^0 \mathbf{1}(\mathbf{r})$ is independent of Γ^+ .

By (52) and (53), equation (32) can be truncated onto the interface Γ_{AB} only, say

$$\tilde{\mathcal{K}}_{AB} \tilde{u}^s - (\mathcal{K}_{AB}^0 \mathbf{1} + \mathcal{K}_+^0 \mathbf{1}) \tilde{u}^s = \tilde{\mathcal{S}}_{AB} \partial_{\nu_c} \tilde{u}^s, \quad \text{on } \Gamma_{AB}. \quad \text{eq5 (61)}$$

Thus, we define the PML-transformed NtD map $\tilde{\mathcal{N}} = (\tilde{\mathcal{K}}_{AB} - \mathcal{K}_{AB}^0 \mathbf{1} - \mathcal{K}_+^0 \mathbf{1})^{-1} \tilde{\mathcal{S}}_{AB}$, mapping $\partial_{\nu_c} \tilde{u}^s$ to \tilde{u}^s on Γ_{AB} . Numerically discretizing the integral operators in (61) approximates the NtD map $\tilde{\mathcal{N}}$ on Γ_{AB} .

3.3 Fourier transformation of boundary integral equations

Direct high-order discretizations of boundary integral equations are non-trivial and usually expensive for complex geometries in three dimensions. However, for axisymmetric domain Ω^a , applying Fourier transformations converts surface integrals into a series of line integrals and yields an efficient algorithm. Thus, the first step in our discretization scheme is the Fourier transformation.

The n -th azimuthal Fourier mode of generic functions $f(\mathbf{r})$ and $F(\mathbf{r}, \mathbf{r}')$ can be expressed as

$$f_n(r) = \frac{1}{\sqrt{2\pi}} \int_{-\pi}^{\pi} e^{-in\theta} f(\mathbf{r}) d\theta, \quad \text{fmode1 (62)}$$

and

$$F_n(r, r') = \frac{1}{\sqrt{2\pi}} \int_{-\pi}^{\pi} e^{-in(\theta-\theta')} F(\mathbf{r}, \mathbf{r}') d(\theta - \theta'), \quad \text{fmode3 (63)}$$

respectively, where $r = (\rho, z)$ and $r' = (\rho', z')$ are the projections of \mathbf{r} and \mathbf{r}' on the ρ - z half-plane, respectively. Using the convolution formula, the azimuthal Fourier modes of the product function $(fg)(\mathbf{r})$ can be expressed in terms of $f_n(r)$ and $g_n(r)$, say

$$(fg)_n(r) = \frac{1}{\sqrt{2\pi}} \sum_{m=-\infty}^{\infty} f_m(r) g_{n-m}(r). \quad \text{eqcon (64)}$$

According to the PML settings in Section 3.2, the complex transformation $\tilde{\mathbf{r}}(\mathbf{r}) = (\tilde{\rho} \cos \theta, \tilde{\rho} \cos \theta, \tilde{z})$ is independent of θ . Let γ^a denotes the projections of Γ^a on the ρ - z half-plane. The kernels of the operators $\tilde{\mathcal{S}}(\mathbf{r}, \mathbf{r}')$, $\tilde{\mathcal{K}}(\mathbf{r}, \mathbf{r}')$ and $\tilde{\mathcal{K}}^0(\mathbf{r}, \mathbf{r}')$ are denoted by $\tilde{S}(r, r')$, $\tilde{K}(r, r')$ and $\tilde{K}^0(r, r')$, respectively. For any $n \in \mathbb{Z}$, integration of (26) yields

$$\tilde{\mathcal{K}}_n \tilde{u}_n^s - \frac{1}{\sqrt{2\pi}} [(\tilde{\mathcal{K}}^0 \mathbf{1}) \tilde{u}^s]_n = \tilde{\mathcal{S}}_n \partial_{\nu_c} \tilde{u}_n^s, \quad \text{on } \gamma^a, \quad \text{eqntd1pm1 (65)}$$

where

$$(\tilde{\mathcal{S}}_n \varphi)(r) = 2 \int_{\gamma^a} \tilde{S}_n(r, r') \varphi(r') \rho' ds(r'), \quad \text{eqsnpm1 (66)}$$

$$(\tilde{\mathcal{K}}_n \varphi)(r) = 2 \int_{\gamma^a} \tilde{K}_n(r, r') \varphi(r') \rho' ds(r'), \quad \text{eqknpm1 (67)}$$

$$(\tilde{\mathcal{K}}_n^0 \varphi)(r) = 2 \int_{\gamma^a} \tilde{K}_n^0(r, r') \varphi(r') \rho' ds(r'), \quad \text{eqk0pm1 (68)}$$

with $\tilde{S}_n(r, r')$, $\tilde{K}_n(r, r')$ and $\tilde{K}_n^0(r, r')$ denote the n -th azimuthal Fourier modes of $\tilde{S}(\mathbf{r}, \mathbf{r}')$, $\tilde{K}(\mathbf{r}, \mathbf{r}')$ and $\tilde{K}^0(\mathbf{r}, \mathbf{r}')$, respectively. Using the convolution formula and the transform

$$(\tilde{\mathcal{K}}^0 1)_n(r) = \sqrt{2\pi}(\tilde{\mathcal{K}}_n^0 1_n)(r) = \delta_{n0}(\tilde{\mathcal{K}}^0 1)_0(r), \quad (69)$$

equation (65) becomes

$$\tilde{\mathcal{K}}_n \tilde{u}_n^s - \frac{1}{2\pi}(\tilde{\mathcal{K}}^0 1)_0 \tilde{u}_n^s = \tilde{\mathcal{S}}_n \partial_{\nu_c} \tilde{u}_n^s, \quad \text{on } \gamma^a. \quad \text{eqntd1pm11} \quad (70)$$

Similarly, integrating equation (61) yields

$$\tilde{\mathcal{K}}_{n,AB} \tilde{u}_n^s - \frac{1}{2\pi}(\mathcal{K}_{AB}^0 1 + \mathcal{K}_{+1}^0 1)_0 \tilde{u}_n^s = \tilde{\mathcal{S}}_{n,AB} \partial_{\nu_c} \tilde{u}_n^s, \quad \text{on } \gamma_{AB}. \quad \text{eqntd1pm12} \quad (71)$$

where $\tilde{\mathcal{K}}_{n,AB}$, $\mathcal{K}_{n,AB}^0$ and $\tilde{\mathcal{S}}_{n,AB}$ are analogous to $\tilde{\mathcal{K}}_n$, \mathcal{K}_n^0 and $\tilde{\mathcal{S}}_n$, respectively, but with the integral domain γ^a replaced by γ_{AB} . It is worth noting that $\mathcal{K}_{+1}^0 1(\mathbf{r})$ is a known function and independent of θ . So we let $R(r)$ denotes the function $\frac{1}{2\pi}(\mathcal{K}_{+1}^0 1(\mathbf{r}))_0$. Consequently, the integral (71) becomes

$$\tilde{\mathcal{K}}_{n,AB} \tilde{u}_n^s - \left(\frac{1}{2\pi}(\mathcal{K}_{AB}^0 1)_0(r) + R(r)\right) \tilde{u}_n^s = \tilde{\mathcal{S}}_{n,AB} \partial_{\nu_c} \tilde{u}_n^s, \quad \text{on } \gamma_{AB}. \quad \text{eq6} \quad (72)$$

From (72), we define the PML-transformed NtD map $\tilde{\mathcal{N}}_n = (\tilde{\mathcal{K}}_{n,AB} \tilde{u}_n^s - \frac{1}{2\pi}(\mathcal{K}_{AB}^0 1)_0(r) - R(r))^{-1} \tilde{\mathcal{S}}_{n,AB}$, mapping $\partial_{\nu_c} \tilde{u}_n^s$ to \tilde{u}_n^s on γ_{AB} . Numerically discretizing the integral operators in (72) approximates the NtD map $\tilde{\mathcal{N}}_n$ on γ_{AB} .

4 Numerical implementation

In this section, we consider the numerical discretizations of integral operators $\tilde{\mathcal{K}}_{n,AB}$, $\tilde{\mathcal{S}}_{n,AB}$ and $(\mathcal{K}_{AB}^0 1)_0$ on γ_{AB} . Let $r(s) = \{(\rho(s), z(s)) | 0 \leq s \leq L_{AB}\}$ represent the parametric equation for γ_{AB} , where s denotes the arclength parameter, and L_{AB} is the length of γ_{AB} . Since corners or edges may exist at the interface of the layered media, the derivatives of \tilde{u}_n^s may exhibit corner singularities. Following [12], we address these singularities through a graded mesh using a scaling function $s = \xi(t)$, $0 \leq t \leq 1$. Specifically, for a smooth segment of the piecewise smooth curve γ_{AB} corresponding to $s \in [s^0, s^1]$ and $t \in [t^0, t^1]$ such that $s^l = \xi(t^l)$, $l = 1, 2$, where s^0 and s^1 correspond to two corners, we take

$$s = \xi(t) = \frac{s^0 \xi_1^p + s^1 \xi_2^p}{\xi_1^p + \xi_2^p}, \quad t \in [t^0, t^1], \quad \text{eqsx1} \quad (73)$$

where

$$\xi_1 = \left(\frac{1}{2} - \frac{1}{p}\right) \xi^3 + \frac{\xi}{p} + \frac{1}{2}, \quad \xi_2 = 1 - \xi_1, \quad \xi = \frac{2t - (t^0 + t^1)}{t^1 - t^0}. \quad (74)$$

Note that p has been used in (17) to define σ_1 , and derivatives of $\xi(t)$ vanish at the corners up to order $p - 1$. Points $t \in [0, 1]$ are discretized by $\{t_j = jh\}_{j=1}^N$ with grid size $h = 1/(N - 1)$, where N is the number of discrete points, including corner points. The function $s = \xi(t)$ creates a graded mesh on γ_{AB} , creating discrete points that cluster near the corner points.

To simplify the notations, we use $r(t)$ to denote $r(\xi(t))$ and $r'(t)$ to denote $\frac{dr}{ds}(\xi(t))\xi'(t)$ in the following.

4.1 Approximating $\tilde{\mathcal{N}}_n$ on γ_{AB}

To obtain an accurate discretization scheme, we first consider the exact evaluation of the PML-transformed modal Green's function. Recall that the kernels of operators $\tilde{\mathcal{S}}(\mathbf{r}, \mathbf{r}')$ and $\tilde{\mathcal{K}}(\mathbf{r}, \mathbf{r}')$ are denoted by $\tilde{S}(\mathbf{r}, \mathbf{r}')$ and $\tilde{K}(\mathbf{r}, \mathbf{r}')$, respectively. These kernels exhibit weakly singularity at $\mathbf{r} = \mathbf{r}'$. To extract the most singular term of the kernels, we split $\tilde{S}(\mathbf{r}, \mathbf{r}')$ and $\tilde{K}(\mathbf{r}, \mathbf{r}')$ as

$$\begin{aligned}\tilde{S}(\mathbf{r}, \mathbf{r}') &= Z(\tilde{\mathbf{r}}, \tilde{\mathbf{r}}') (H_1(\tilde{\mathbf{r}}, \tilde{\mathbf{r}}') + \mathbf{i}H_2(\tilde{\mathbf{r}}, \tilde{\mathbf{r}}')), & \text{eq:s1} \\ \tilde{K}(\mathbf{r}, \mathbf{r}') &= D(\tilde{\mathbf{r}}, \tilde{\mathbf{r}}') (H_3(\tilde{\mathbf{r}}, \tilde{\mathbf{r}}') + \mathbf{i}H_4(\tilde{\mathbf{r}}, \tilde{\mathbf{r}}')), & \text{eq:k1}\end{aligned}$$

where $\tilde{\mathbf{r}} = (\tilde{\rho} \cos \theta, \tilde{\rho} \sin \theta, \tilde{z})$, $\tilde{\mathbf{r}}' = (\tilde{\rho}' \cos \theta', \tilde{\rho}' \sin \theta', \tilde{z}')$,

$$\begin{aligned}Z(\tilde{\mathbf{r}}, \tilde{\mathbf{r}}') &= \frac{1}{4\pi |\tilde{\mathbf{r}} - \tilde{\mathbf{r}}'|}, \\ D(\tilde{\mathbf{r}}, \tilde{\mathbf{r}}') &= -\frac{\nu'_{c,\rho} (\tilde{\rho}' - \tilde{\rho} \cos(\theta - \theta')) + \nu'_{c,z} (\tilde{z}' - \tilde{z})}{4\pi |\tilde{\mathbf{r}} - \tilde{\mathbf{r}}'|^3}, \\ H_1(\tilde{\mathbf{r}}, \tilde{\mathbf{r}}') &= \cos(\omega_1 |\tilde{\mathbf{r}} - \tilde{\mathbf{r}}'|), \\ H_2(\tilde{\mathbf{r}}, \tilde{\mathbf{r}}') &= \sin(\omega_1 |\tilde{\mathbf{r}} - \tilde{\mathbf{r}}'|), \\ H_3(\tilde{\mathbf{r}}, \tilde{\mathbf{r}}') &= \cos(\omega_1 |\tilde{\mathbf{r}} - \tilde{\mathbf{r}}'|) + \omega_1 |\tilde{\mathbf{r}} - \tilde{\mathbf{r}}'| \sin(\omega_1 |\tilde{\mathbf{r}} - \tilde{\mathbf{r}}'|), \\ H_4(\tilde{\mathbf{r}}, \tilde{\mathbf{r}}') &= \sin(\omega_1 |\tilde{\mathbf{r}} - \tilde{\mathbf{r}}'|) - \omega_1 |\tilde{\mathbf{r}} - \tilde{\mathbf{r}}'| \cos(\omega_1 |\tilde{\mathbf{r}} - \tilde{\mathbf{r}}'|).\end{aligned}$$

Integrating both sides of equations (75) and (76) gives

$$\begin{aligned}\tilde{S}_n(r, r') &= (ZH_1)_n(\tilde{r}, \tilde{r}') + \mathbf{i}(ZH_2)_n(\tilde{r}, \tilde{r}'), & \text{eqs:nsp1} \\ \tilde{K}_n(r, r') &= (DH_3)_n(\tilde{r}, \tilde{r}') + \mathbf{i}(DH_4)_n(\tilde{r}, \tilde{r}'). & \text{eqk:nsp1}\end{aligned}$$

Here, $\tilde{r} = (\tilde{\rho}, \tilde{z})$ and $\tilde{r}' = (\tilde{\rho}', \tilde{z}')$ are the projections of $\tilde{\mathbf{r}}$ and $\tilde{\mathbf{r}}'$ in the ρ - z half-plane, respectively.

Clearly, the distance function $|\tilde{\mathbf{r}} - \tilde{\mathbf{r}}'|$ is complex-valued. When \tilde{r} and \tilde{r}' are well-separated, the kernels $S_n(\tilde{r}, \tilde{r}')$ and $K_n(\tilde{r}, \tilde{r}')$ are computed via FFT in the azimuthal direction. When \tilde{r} and \tilde{r}' are close, the function H_1, H_3, ZH_2, DH_4 are smooth while $H_2, H_4, Z, ZH_1, D, DH_3$ are non-smooth. For a smooth function $f(\mathbf{r})$, its Fourier mode $f_n(\tilde{r})$ decays rapidly with n and converges rapidly with discrete points number N in the FFT. Therefore, the functions $(ZH_2)_n(\tilde{r}, \tilde{r}')$ and $(DH_4)_n(r, r')$ are computed via FFT. Since the Fourier mode of $fg(\tilde{r})$ has a rapid convergence if at least one series of $f_n(\tilde{r})$ and $g_n(r)$ decays rapidly, the functions $(ZH_1)_n(\tilde{r}, \tilde{r}')$ and $(DH_3)_n(\tilde{r}, \tilde{r}')$ are computed via convolution. For the convolution of the functions $(ZH_1)_n(\tilde{r}, \tilde{r}')$ and $(DH_3)_n(\tilde{r}, \tilde{r}')$, the required functions $Z_n(\tilde{r}, \tilde{r}')$ and $D_n(\tilde{r}, \tilde{r}')$ are evaluated by semi-analytical techniques and special functions. See [17, 15, 25] for further details on the approximation of the functions $Z_n(\tilde{r}, \tilde{r}')$ and $D_n(\tilde{r}, \tilde{r}')$.

Next, we discretize the integral equation along the generating curve γ_{AB} . Since the modal Green's functions possess logarithmic singularities [13], our discretization scheme is based on the hybrid Gauss-trapezoidal quadrature rules developed by Alpert [2]. The operators $\tilde{\mathcal{S}}_{n,AB}$ and $\tilde{\mathcal{K}}_{n,AB}$ at $r = r(t_l)$, $l = 1, \dots, N$, can be parameterized by

$$\begin{aligned}\tilde{\mathcal{S}}_{n,AB}(\partial_{\nu_c} \tilde{u}_n^s)(r(t_l)) &= \int_0^1 \tilde{S}_n(r(t_l), r(t)) \varphi(t) dt, & \text{eqsnab} \\ \tilde{\mathcal{K}}_{n,AB}(\tilde{u}_n^s)(r(t_l)) &= \int_0^1 \tilde{K}_n(r(t_l), r(t)) \tilde{u}_n^s dt, & (80)\end{aligned}$$

where $\varphi(t) = \partial_{\nu_c} \tilde{u}_n^s |r'(t)|$. Taking $\tilde{\mathcal{S}}_{n,AB}(\partial_{\nu_c} \tilde{u}_n^s)(r(t_l))$ as an example, the integrand in (79) have logarithmic singularities at t_l . Therefore, we rewrite (79) as

$$\tilde{\mathcal{S}}_{n,AB}(\partial_{\nu_c} \tilde{u}_n^s)(r(t_l)) = \int_0^{t_l} \tilde{S}_n(r(t_l), r(t)) \varphi(t) dt + \int_{t_l}^1 \tilde{S}_n(r(t_l), r(t)) \varphi(t) dt. \quad \text{eqsnab1} \quad (81)$$

Let N_1 and N_2 denote the number of discrete points on intervals $[0, t_l]$ and $[t_l, 1]$, respectively.

By applying Alpert's hybrid Gauss-trapezoidal quadrature rule, the first part of the r.h.s of (81) can be discretized as

$$\begin{aligned} \int_0^{t_l} \tilde{S}_n(r(t_l), r(t)) \varphi(t) dt &\approx \sum_{k=1}^{K_1} \gamma_k h \tilde{S}(t_l, \delta_k h) \varphi(\delta_k h) \\ &+ \sum_{k=1}^{K_2} \gamma'_k h \tilde{S}(t_l, t_l - \delta'_k h) \varphi(t_l - \delta'_k h) \quad \text{eqsnt1} \quad (82) \\ &+ \sum_{k=K_3}^{N_1-K_4} h \tilde{S}(t_l, t_k) \varphi(t_k), \end{aligned}$$

where the values of $K_1, K_2, K_3, K_4, \gamma_k, \gamma'_k, \delta_k$ and δ'_k are depend on the order of Alpert's quadrature rule and can be precomputed. In cases where $N_1 < K_1 + K_2$, the third sum on the r.h.s of (82) becomes irrational. In this situation, we rescaled the interval $[0, t_l]$ with a new grid size $h_1 = 1/(K_1 + K_2 - 1)$, ensuring that the number of uniform nodes on the interval $[0, t_l]$ is at least $K_1 + K_2$. The second sum on the r.h.s of equation (81) can be discretized similarly. For $l = 1, \dots, N$, adopting the Lagrange interpolation formula to approximate $\varphi(\delta_k h), \varphi(t_l - \delta'_k h), \varphi(t_l + \delta'_k h)$ and $\varphi(1 - \delta_k h)$ in terms of $\{\varphi(t_j)\}_{j=1}^N$, we obtain

$$\left(\tilde{\mathcal{S}}_{n,AB} \partial_{\nu_c} \tilde{u}_n^s \right) \begin{bmatrix} r(t_1) \\ \vdots \\ r(t_N) \end{bmatrix} \approx \tilde{\mathbf{S}}_n \begin{bmatrix} \varphi(t_1) \\ \vdots \\ \varphi(t_N) \end{bmatrix}, \quad (83)$$

where $\tilde{\mathbf{S}}_n$ is an $N \times N$ matrix approximating the operator $\tilde{\mathcal{S}}_{n,AB}$. Similarly, an $N \times N$ matrix $\tilde{\mathbf{K}}_n$ that approximates the operator $\tilde{\mathcal{K}}_{n,AB}$ can be derived as

$$\left(\tilde{\mathcal{K}}_{n,AB} \tilde{u}_n^s \right) \begin{bmatrix} r(t_1) \\ \vdots \\ r(t_N) \end{bmatrix} \approx \tilde{\mathbf{K}}_n \begin{bmatrix} \tilde{u}_n^s(r(t_1)) \\ \vdots \\ \tilde{u}_n^s(r(t_N)) \end{bmatrix}. \quad (84)$$

The operator $(\frac{1}{2\pi}(\mathcal{K}_{AB}^0 1)_0(r) + R(r))$ in (72) can be approximated by an $N \times N$ diagonal matrix \mathbf{D} with entries $(\frac{1}{2\pi}(\mathcal{K}_{AB}^0 1)_0(r(t_j)) + R(r(t_j)))$, $j = 1, \dots, N$. Thus, equation (72) can be transformed in matrix equation form as

$$(\tilde{\mathbf{K}}_n - \mathbf{D}) \tilde{u}_n^s \approx \tilde{\mathbf{S}} \varphi_n, \quad (85)$$

where

$$\tilde{u}_n^s = [u_n^s(r(t_1)), \dots, u_n^s(r(t_N))]^T, \quad (86)$$

$$\varphi_n = [\varphi_n(r(t_1)), \dots, \varphi_n(r(t_N))]^T. \quad (87)$$

Consequently, one gets

$$\tilde{u}_n^s \approx \tilde{\mathbf{N}}_n \varphi_n := (\tilde{\mathbf{K}}_n - \mathbf{D})^{-1} \tilde{\mathbf{S}} \varphi_n \quad (88)$$

where the $N \times N$ matrix $\tilde{\mathbf{N}}_n$ approximates the NtD operator $\tilde{\mathcal{N}}_n$ mapping $\varphi_n = |r'| \partial_{\nu_c} \tilde{u}_n$ to \tilde{u}_n^s on γ_{AB} .

4.2 Wave field evaluations

Suppose now for each domain Ω_j , we have obtained an $N \times N$ matrices $\tilde{\mathbf{N}}_n^j$ approximating the NtD operator $\tilde{\mathcal{N}}_n^j$ mapping $|r'| \partial_{\nu_c} \tilde{\mathbf{u}}_n^{s,j}$ to $\tilde{\mathbf{u}}_n^{s,j}$ on γ_{AB} for $j = 1, 2$. Thus, we obtain the following relation

$$\tilde{\mathbf{u}}_n^{s,j} = \tilde{\mathbf{N}}_n^j \boldsymbol{\varphi}_n^j, \quad j = 1, 2, \quad \text{eqntdnj} \quad (89)$$

where

$$\mathbf{u}_n^{s,j} = [u_n^{s,j}(r(t_1)), \dots, u_n^{s,j}(r(t_N))]^T, \quad (90)$$

$$\boldsymbol{\varphi}_n^j = [\varphi_n^j(r(t_1)), \dots, \varphi_n^j(r(t_N))]^T, \quad (91)$$

and $\varphi_n^j = |r'| \partial_{\nu_c} \tilde{\mathbf{u}}_n^{s,j}$.

Applying the transmission conditions (13) and (14), the scattering wave field $\tilde{\mathbf{u}}_n^{s,j}$ on γ_{AB} satisfies

$$\tilde{\mathbf{u}}_n^{s,1} - \tilde{\mathbf{u}}_n^{s,2} = \mathbf{b}_n^1, \quad (92)$$

$$\boldsymbol{\varphi}_n^1 - \boldsymbol{\varphi}_n^2 = \mathbf{b}_n^2, \quad (93)$$

where

$$\mathbf{b}_n^1 = [- [\tilde{u}_n^{tot,0}] (r(t_1)), \dots, - [\tilde{u}_n^{tot,0}] (r(t_N))]^T,$$

$$\mathbf{b}_n^2 = [- |r'(t_1)| [\partial_{\nu_c} \tilde{u}_n^{tot,0}] (r(t_1)), \dots, - |r'(t_N)| [\partial_{\nu_c} \tilde{u}_n^{tot,0}] (r(t_N))]^T,$$

and $\tilde{u}_n^{tot,0}$ denotes the n -th Fourier mode of $\tilde{u}^{tot,0}$, which is the PML-transformed wave field of the reference wave field $u^{tot,0}$. From equation (89), we obtain

$$\begin{bmatrix} \tilde{\mathbf{N}}_n^1 & -\tilde{\mathbf{N}}_n^2 \\ \mathbf{I} & -\mathbf{I} \end{bmatrix} \begin{bmatrix} \boldsymbol{\varphi}_n^1 \\ \boldsymbol{\varphi}_n^2 \end{bmatrix} = \begin{bmatrix} \mathbf{b}_n^1 \\ \mathbf{b}_n^2 \end{bmatrix}, \quad (94)$$

where \mathbf{I} denotes the identity matrix and the solution

$$\boldsymbol{\varphi}_n^1 = (\tilde{\mathbf{N}}_n^1 - \tilde{\mathbf{N}}_n^2)^{-1} (\mathbf{b}_n^1 - \tilde{\mathbf{N}}_n^2 \mathbf{b}_n^2), \quad \text{eqntdpsi1} \quad (95)$$

$$\boldsymbol{\varphi}_n^2 = \boldsymbol{\varphi}_n^1 - \mathbf{b}_n^2. \quad \text{eqntdpsi2} \quad (96)$$

Then, we obtain the scattering wave $\tilde{\mathbf{u}}_n^{s,j} = \tilde{\mathbf{N}}_n^j \boldsymbol{\varphi}_n^j$, for $j = 1, 2$, on γ_{AB} . For $r \in \Omega_j$, using Green's representation formula, the scattering wave field is approximated as

$$\tilde{\mathbf{u}}_n^{s,j}(r) \approx \int_{\gamma_{AB}} \left\{ \tilde{G}_j(r, r') \partial_{\nu_c} \tilde{\mathbf{u}}_n^{s,j}(r') - \partial_{\nu_c} \tilde{G}_j(r, r') \tilde{\mathbf{u}}_n^{s,j}(r') \right\} ds(r'). \quad \text{eqfujs} \quad (97)$$

After parameterizing by the scaling function $s = w(t)$ from (73), the integral in (97) becomes sufficiently smooth. Applying the trapezoidal rule yields

$$\begin{aligned} \tilde{\mathbf{u}}_n^{s,j}(r) \approx & \frac{1}{N} \sum_{l=1}^N [\tilde{G}_j(r, r(t_l)) |r'(t_l)| \partial_{\nu_c} \tilde{\mathbf{u}}_n^{s,j}(r(t_l)) \\ & - \partial_{\nu_c} \tilde{G}_j(r, r(t_l)) |r'(t_l)| \tilde{\mathbf{u}}_n^{s,j}(r(t_l))]. \end{aligned} \quad (98)$$

The scattered field is then given by $\mathbf{u}_n^{s,j} = \tilde{\mathbf{u}}_n^{s,j}$. Consequently, in the physical domain outside the PML layer, the complete total wave field is obtained as

$$\mathbf{u}^{tot,j} = \mathbf{u}^{tot,0} + \mathbf{u}^{s,j}, \quad \text{in } \Omega_j, \quad (99)$$

where $j = 1, 2$ and $\mathbf{u}^{s,j} = \sum_{n=-\infty}^{\infty} \mathbf{u}_n^{s,j}$.

4.3 Instability issues

In this subsection, we address several instability issues that arise during numerical computations and propose strategies to tackle them. When evaluating the kernel functions $\tilde{S}_n(r, r')$ and $\tilde{K}_n(r, r')$, if r is very close to r' or close to the boundary, the distant function $|\tilde{\mathbf{r}} - \tilde{\mathbf{r}}'|$ utilized in FFT may tend to zero, leading to numerical instabilities or potential divide-by-zero errors. To resolve these instabilities, we rewrite the distant function

$$\begin{aligned} |\tilde{\mathbf{r}} - \tilde{\mathbf{r}}'| &= \sqrt{\tilde{\rho}^2 + \tilde{\rho}'^2 - 2\tilde{\rho}\tilde{\rho}' + 4\tilde{\rho}\tilde{\rho}' \sin^2\left(\frac{\theta - \theta'}{2}\right) + (\tilde{z} - \tilde{z}')^2} \\ &= \sqrt{|\tilde{\mathbf{r}} - \tilde{\mathbf{r}}'|^2 + 4\tilde{\rho}\tilde{\rho}' \sin^2\left(\frac{\theta - \theta'}{2}\right)}, \end{aligned}$$

Following the stabilization technique detailed in Section 4.3 of [20], we can compute $|\tilde{\mathbf{r}} - \tilde{\mathbf{r}}'|$ accurately. Since the values of functions $|\tilde{\mathbf{r}} - \tilde{\mathbf{r}}'|$ and $4\tilde{\rho}\tilde{\rho}' \sin^2\left(\frac{\theta - \theta'}{2}\right)$ are both positive numbers, there are no significant rounding error. A similar approach was used to accurately evaluate $D(\tilde{\mathbf{r}}, \tilde{\mathbf{r}}')$.

Another instability issue arises during the convolution of the functions $(ZH_1)_n(\tilde{\mathbf{r}}, \tilde{\mathbf{r}}')$ and $(DH_3)_n(\tilde{\mathbf{r}}, \tilde{\mathbf{r}}')$. In the PML region, as $\theta \in [0, 2\pi)$ varies, the positive imaginary part of the value for distance function $|\tilde{\mathbf{r}} - \tilde{\mathbf{r}}'|$ may become large so that the functions $H_1(\tilde{\mathbf{r}}, \tilde{\mathbf{r}}')$ and $H_3(\tilde{\mathbf{r}}, \tilde{\mathbf{r}}')$ grow exponentially, which leads to the series $H_{1n}(\tilde{\mathbf{r}}, \tilde{\mathbf{r}}')$ and $H_{3n}(\tilde{\mathbf{r}}, \tilde{\mathbf{r}}')$ converging at a slow rate. To overcome this problem, we introduce rapidly converging functions to replace the functions $H_1(\tilde{\mathbf{r}}, \tilde{\mathbf{r}}')$ and $H_3(\tilde{\mathbf{r}}, \tilde{\mathbf{r}}')$. Let the functions $H_1(\tilde{\mathbf{r}}, \tilde{\mathbf{r}}')$ and $H_3(\tilde{\mathbf{r}}, \tilde{\mathbf{r}}')$ be denoted by $H_1(q)$ and $H_3(q)$, respectively, where $q = \omega|\tilde{\mathbf{r}} - \tilde{\mathbf{r}}'|$ is a complex number with a positive imaginary part. For simplicity, we consider the function $H_1(q)$ only. Applying the constant transformation

$$H_1(q) = H_1(q)e^{-iq}e^{iq}, \quad (100)$$

the truncated Taylor expansion of the function $H_1(q)e^{-iq}$ is given by

$$H_1(q)e^{-iq} = \sum_{k=0}^L a_k z^k + O(q^{L+1}), \quad (101)$$

where L denotes the truncation parameter. We define the function

$$cH_1(q, L) = e^{iq} \sum_{k=0}^L a_k z^k. \quad \text{eqch1} \quad (102)$$

Let the function $H_1(q)$ be replaced by the function $cH_1(q, L)$, which exhibits enhanced convergence properties. Accordingly, we replace $iH_2(q)$ with $e^{iq} - cH_1(q, L)$ to minimize the error raised by substitution.

To illustrate the efficiency of this replacement, we carry out a specific experiment to validate the necessity of using the function $cH_1(q, L)$. As illustrated in Figure 2(b), the surface Γ_{AB} is generated by rotating the line γ_{AB} with endpoints \mathbf{V} given by

$$\mathbf{V} = \{(0, -1), (1, -1), (1, 0), (4, 0)\}.$$

we set $\omega_1 = \omega_2 = 2\pi$, $n = 1$, $a_1 = 2$, the PML thickness $T = 2$, and the PML parameter $S = 2$. We have two choices to evaluate the kernel functions $\tilde{S}_n(r, r')$ and $\tilde{K}_n(r, r')$, where $q = \omega_1|\tilde{\mathbf{r}} - \tilde{\mathbf{r}}'|$. First, using the original functions $H_1(q)$ and $H_3(q)$ to evaluate the kernel

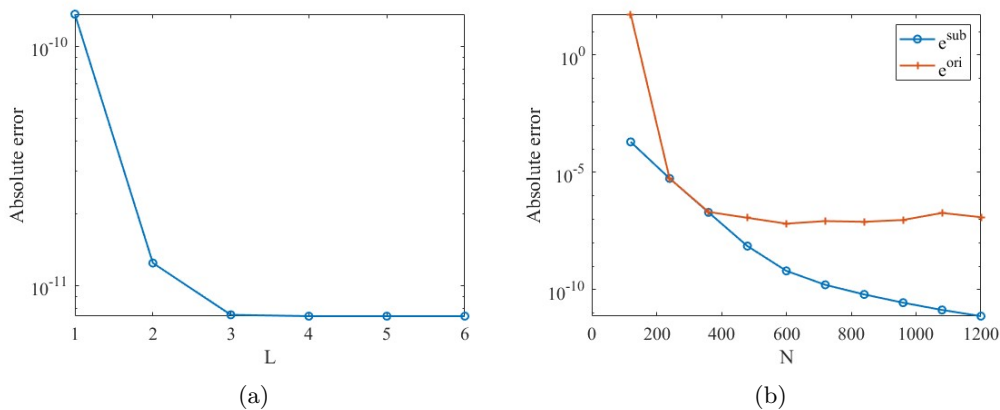


Figure 4. (a) Accuracy of the NtD matrix N_n^{sub} for varying L . (b) Accuracy of the two NtD matrices N_n^{ori} and N_n^{sub} , for $L = 5$. picntde

functions $\tilde{S}_n(r, r')$ and $\tilde{K}_n(r, r')$, respectively, we obtain an $N \times N$ matrix \tilde{N}_n denoted by \tilde{N}_n^{ori} . Second, we substitute the functions $cH_1(q, L)$ and $cH_3(q, L)$ for the original functions $H_1(q)$ and $H_3(q)$, respectively, to obtain the NtD matrix \tilde{N}_n^{sub} .

To compare the accuracy of the two NtD matrices, we employ the following explicit solution

$$\tilde{u}(\mathbf{r}) = \tilde{S}(\mathbf{r}, \mathbf{r}_p) = \frac{e^{i\omega_1|\tilde{\mathbf{r}}-\tilde{\mathbf{r}}_p|}}{4\pi|\tilde{\mathbf{r}}-\tilde{\mathbf{r}}_p|}, \quad (103)$$

with $\mathbf{r}_p = (0.5, 0, -1.3)$. Thus, the excited fields \tilde{u}_n and the normal derivative $\partial_\nu \tilde{u}_n$ are given by

$$\tilde{u}_n(r) = \tilde{S}_n(r, r_p), \quad \partial_\nu \tilde{u}_n(r) = \tilde{K}_n(r, r_p), \quad r \in \gamma_{AB}. \quad (104)$$

The corresponding errors are defined as

$$e^i = \|\mathbf{u}_n - \tilde{N}_n^i \boldsymbol{\varphi}_n\|_2, \quad i \in \{\text{ori}, \text{sub}\}. \quad (105)$$

For $N = 1200$, we plot the error function with varying L in Figure 4(a). Accurate results can be produced even with a small L , and for convenience, we set $L = 5$ in the following. The absolute errors of the two error functions against the number of discretization points N are shown in Figure 4(b). Numerical results validate the necessity of using the function $cH_1(q, L)$.

5 Numerical examples

In this section, we present several numerical experiments to illustrate the efficiency of our algorithm. The physical domain is defined as $\Omega_{phy} = \{(\rho, \theta, z) | \rho \leq a_1, 0 \leq \theta < 2\pi, |z| \leq a_2\}$. Since the integration domain γ_{AB} is independent of a_2 , we let a_2 approach infinity. Therefore, the PML domain $\Omega_{pml} = \{(\rho, \theta, z) | a_1 \leq \rho \leq a_1 + T, a_1 > 0, T > 0\}$.

In all examples, we take $p = 6$ to define σ_1 and the scaling function $\xi(t)$, and apply Alpert's quadrature rule of the 10-th order to discretize the integral equations. And we set $\omega_1 = 2\pi$, $\omega_2 = 2.4\pi$, $a_1 = 2$. In the following, we consider two kinds of incident waves: a plane wave incidence with the incident angle $\phi^{inc} = \pi/3$, $\theta^{inc} = 0$, and a spherical wave incidence excited by the source $r^* = (0.3, 0, 0.5)$.

Example 1. In this example, we consider a perturbation with a rectangular cross-section, as shown in Figure 6(a). The depth and radius of the perturbation are both set to

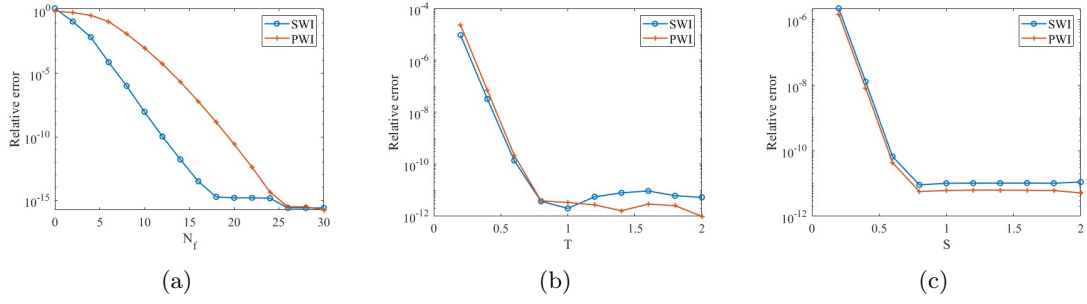


Figure 5. Result for Example 1 with $N = 800$. (a) Relative errors of $cu^{s,j}$ with respect to N_f . (b) Relative errors of u^{tot} against T for $S = 2$. (c) Relative errors of u^{tot} against S for $T = 2$. SWI: Spherical wave incidence, PWI: Plane wave incidence. fg5

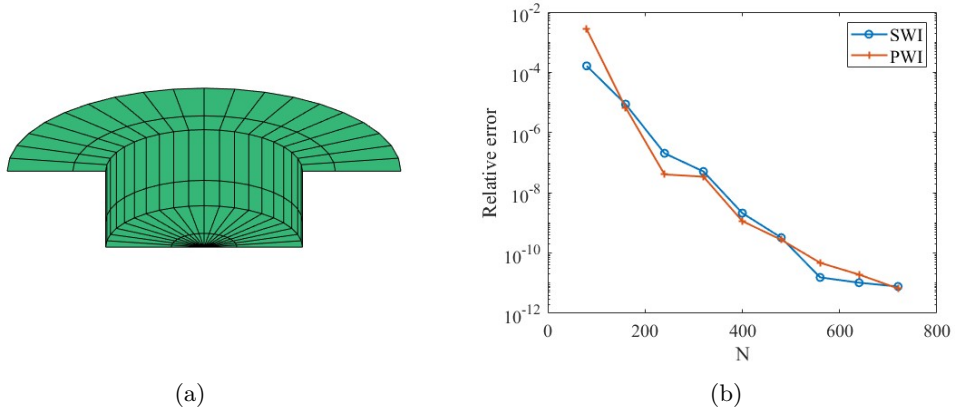


Figure 6. Result for Example 1. (a) Illustration of the perturbation. (b) Relative errors against N for $T = 2$ and $S = 2$. fg4

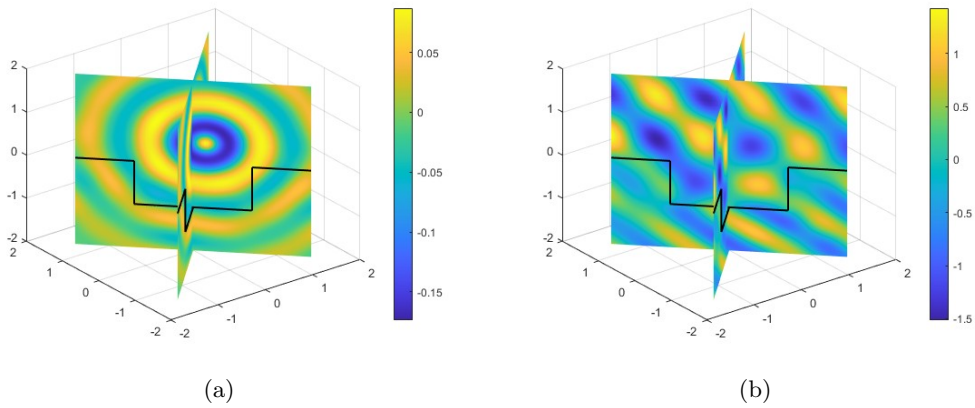


Figure 7. Result for Example 1. (a) and (b) are the real parts of the scattered field for spherical and plane wave incidences, respectively. fg9

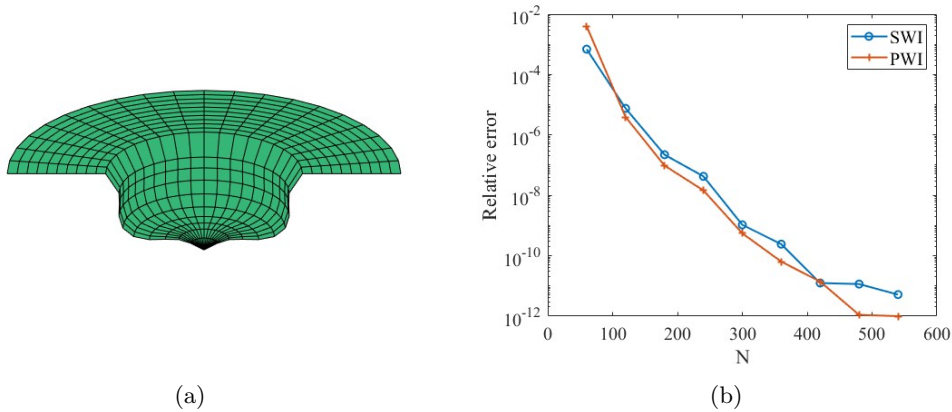


Figure 8. Result for Example 2. (a) Illustration of the perturbation. (b) Relative errors against N for $T = 2$ and $S = 2$. fg6

1. First, we investigate the convergence of the Fourier modes of the scattered field $\mathbf{u}^{s,j} = \sum_{n=-\infty}^{\infty} \mathbf{u}_n^{s,j}$. Let the truncated scattered field be denoted by $\mathbf{c}\mathbf{u}^{s,j} = \sum_{n=-N_f}^{N_f} \mathbf{u}_n^{s,j}$, where N_f denotes the truncation parameter. We set the number of discrete points $N = 800$, the PML thickness $T = 2$ and the PML parameter $S = 2$. For the case of spherical wave incidence, we compute $\mathbf{c}\mathbf{u}^{s,j}$ for different values of N_f ranging from 0 to 32. Using the numerical solution $\mathbf{c}\mathbf{u}^{s,j}$ with $N_f = 32$ as a reference, we compute the relative errors for the less accurate numerical solutions with lower N_f . Similarly, for plane wave incidence, using $\mathbf{c}\mathbf{u}^{s,j}$ with $N_f = 32$ as a reference solution to compute the relative errors for lower N_f . The numerical results are shown in Figure 5(a). We can observe that the truncated scattered fields $\mathbf{c}\mathbf{u}^{s,j}$ for two types of wave incidence converge rapidly as N_f increases. Therefore, we let $\mathbf{u}^{s,j} = \sum_{n=-N_f}^{N_f} \mathbf{u}_n^{s,j}$. In the following, we set the Fourier truncation parameters to $N_f = 20$ and $N_f = 30$ for the spherical and plane wave incidence cases, respectively.

Next, we investigate the convergence of the scattered field \mathbf{u}^{tot} as the PML thickness T and the PML parameter S vary. Let $N = 800$. For both spherical and plane wave incidences, the reference solutions are the total wave field \mathbf{u}^{tot} for $T = 2.2$. These reference values are utilized to calculate the relative errors for the less accurate numerical solutions with lower T . Numerical results for both incident waves are depicted in Figure 5(b). Similarly, using the solution for $S = 2.2$ as a reference, the relative errors for the less accurate numerical solutions with lower S are shown in Figure 5(c). It can be observed that the relative errors decay exponentially at the beginning and then yield to the discretization error. Those relative errors demonstrate the efficiency of the proposed PML-based BIE solver for three-dimensional problems.

Then, we study the relative errors of \mathbf{u}^{tot} as the number of discrete points N varies. For both spherical and plane wave incidences, the reference solutions are the total wave field \mathbf{u}^{tot} for $N = 800$. These reference values are used to calculate the relative errors for the less accurate numerical solutions with lower N . Numerical results for both incident waves are shown in Figure 6(b). Figure 7 shows the spherical wave scattering with 41 modes and the plane wave scattering with 61 modes at four azimuthal directions, $\theta = \frac{\pi}{4}, \frac{3\pi}{4}, \frac{5\pi}{4}, \frac{7\pi}{4}$.

Example 2. In the second example, we consider an axisymmetric perturbation with

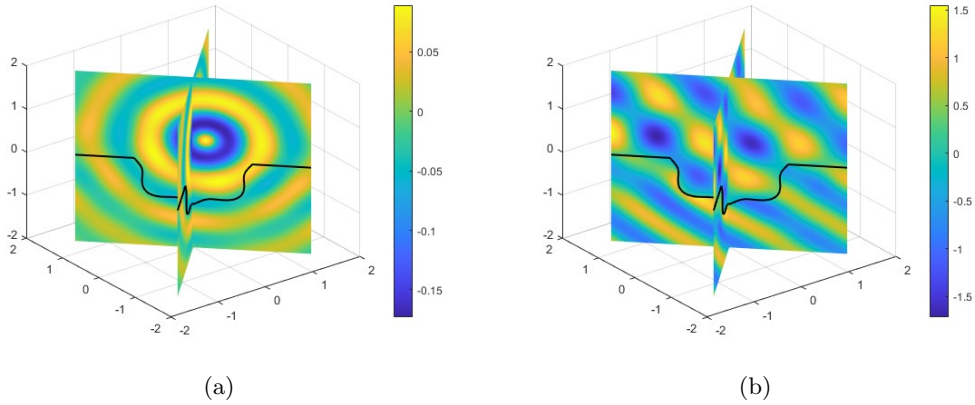


Figure 9. Result for Example 2. (a) and (b) are the real parts of the scattered field for spherical and plane wave incidences, respectively. fg10

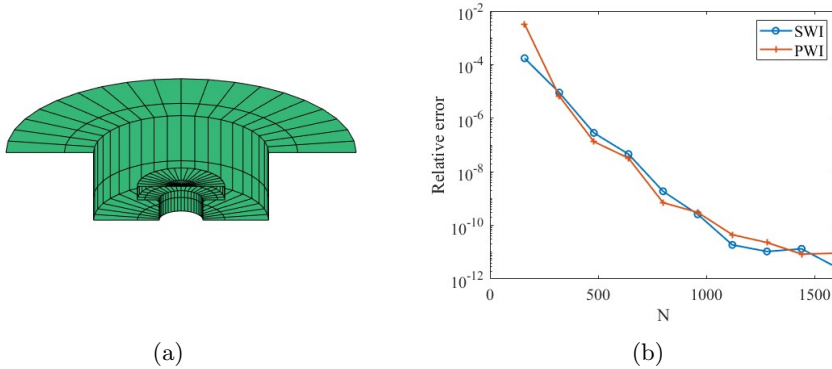


Figure 10. Result for Example 3. (a) Illustration of the perturbation. (b) Relative errors against N for $T = 2$ and $S = 2$. fg7

the generating curve

$$\begin{aligned}\rho(s) &= [1 - 0.1 \sin(3\pi s)] \sin\left(\frac{\pi}{2}s\right), \\ z(s) &= -[1 - 0.1 \sin(3\pi s)] \cos\left(\frac{\pi}{2}s\right),\end{aligned}\tag{106}$$

for $s \in [0, 1]$, as depicted in 8(a). For two types of incident waves, we employ different values of N_f like Example 1. Using $N = 600$ points to discretize the generating curve γ_{AB} , we obtain a reference wave filed \mathbf{u}^{tot} . The relative errors for the less accurate numerical solutions with lower N are calculated from this reference value. Numerical results for both incident waves are shown in Figure 8(b). The scattered fields for spherical and plane wave incidence are given in Figure 9.

Example 3. In the third example, we consider a perturbation whose generating curve has vertices given by

$$V = \{(0, -0.5), (0.5, -0.5), (0.5, -0.7), (0.25, -0.7), (0.25, -1), (1, -1), (1, 0)\},\tag{107}$$

as shown in Figure 10(a). Each segment of the piecewise smooth is rescaled by the function $\xi(t)$ to resolve the corner singularities. Using $N = 1600$ points to discretize the generating curve γ_{AB} , we obtain a reference wave filed \mathbf{u}^{tot} . The relative errors for the less accurate

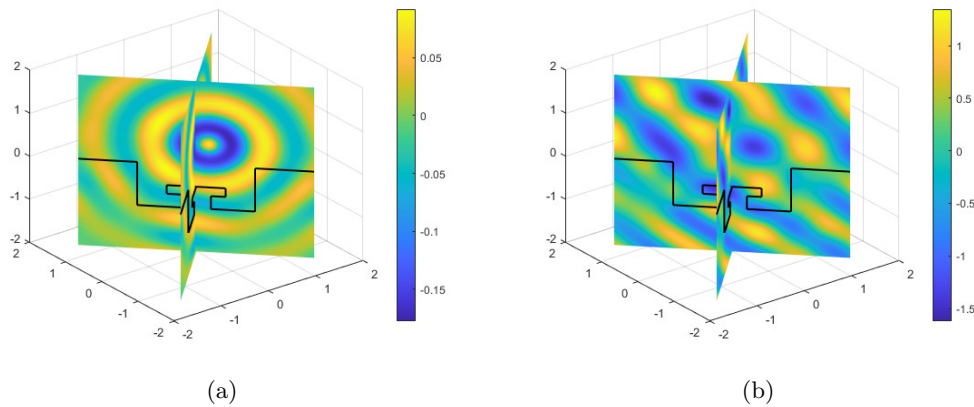


Figure 11. Result for Example 3. (a) and (b) are the real parts of the scattered field for spherical and plane wave incidences, respectively. fg11

numerical solutions with lower N are calculated by this reference value. Numerical results for both incident waves are shown in Figure 10(b). Figure 11 gives the scattered field for spherical and plane wave incidence.

References

- [1] Monro J. A. *A super-algebraically convergent, windowing-based approach to the evaluation of scattering from periodic rough surfaces*. California Institute of Technology, 2008.
- [2] B. K. Alpert. Hybrid gauss-trapezoidal quadrature rules. *SIAM Journal on Scientific Computing*, 20(5):1551–1584, 1999.
- [3] T. Arens and T. Hohage. On radiation conditions for rough surface scattering problems. *IMA Journal of Applied Mathematics*, 70(6):839–847, 12 2005.
- [4] O. Bruno, T. Elling, and C. Turc. Regularized integral equations and fast high-order solvers for sound-hard acoustic scattering problems. *International Journal for Numerical Methods in Engineering*, 91(10):1045–1072, 2012.
- [5] O. P Bruno, M. Lyon, C. Pérez-Arancibia, and C. Turc. Windowed green function method for layered-media scattering. *SIAM Journal on Applied Mathematics*, 76(5):1871–1898, 2016.
- [6] O. P. Bruno and T. Yin. A windowed green function method for elastic scattering problems on a half-space. *Computer Methods in Applied Mechanics and Engineering*, 376:113651, 2021.
- [7] W. Cai. Algorithmic issues for electromagnetic scattering in layered media: Green’s functions, current basis, and fast solver. *Advances in Computational Mathematics*, 16:157–174, 2002.
- [8] S. N. Chandler-Wilde and B. Zhang. A uniqueness result for scattering by infinite rough surfaces. *SIAM Journal on Applied Mathematics*, 58(6):1774–1790, 1998.

- [9] Z. Chen and W. Zheng. Convergence of the uniaxial perfectly matched layer method for time-harmonic scattering problems in two-layered media. *SIAM Journal on Numerical Analysis*, 48(6):2158–2185, 2010.
- [10] W. C. Chew. *Waves and fields in inhomogeneous media*, volume 16. John Wiley & Sons, 1999.
- [11] W. C. Chew and W. H. Weedon. A 3d perfectly matched medium from modified maxwell’s equations with stretched coordinates. *Microwave and Optical Technology Letters*, 7(13):599–604, 1994.
- [12] D. Colton and R. Kress. *Inverse Acoustic and Electromagnetic Scattering Theory*. Applied Mathematical Sciences. Springer Berlin Heidelberg, 2013.
- [13] J. T. Conway and H. S. Cohl. Exact fourier expansion in cylindrical coordinates for the three-dimensional helmholtz green function. *Zeitschrift für angewandte Mathematik und Physik*, 61:425–443, 2010.
- [14] Y. Gao and W. Lu. Wave scattering in layered orthotropic media i: a stable pml and a high-accuracy boundary integral equation method. *SIAM Journal on Scientific Computing*, 44(4):B861–B884, 2022.
- [15] J. Helsing and A. Karlsson. An explicit kernel-split panel-based nyström scheme for integral equations on axially symmetric surfaces. *Journal of Computational Physics*, 272:686–703, 09 2014.
- [16] J. Helsing and A. Karlsson. Resonances in axially symmetric dielectric objects. *IEEE Transactions on Microwave Theory and Techniques*, 65(7):2214–2227, July 2017.
- [17] J. Lai and M. O’Neil. An fft-accelerated direct solver for electromagnetic scattering from penetrable axisymmetric objects. *Journal of Computational Physics*, 390:152–174, 2019.
- [18] M. Lassas and E. Somersalo. Analysis of the pml equations in general convex geometry. *Proceedings of the Royal Society of Edinburgh: Section A Mathematics*, 131:1183 – 1207, 10 2001.
- [19] W. Lu. Mathematical analysis of wave radiation by a step-like surface. *SIAM Journal on Applied Mathematics*, 81(2):666–693, 2021.
- [20] W. Lu, Y. Y. Lu, and J. Qian. Perfectly matched layer boundary integral equation method for wave scattering in a layered medium. *SIAM Journal on Applied Mathematics*, 78(1):246–265, 2018.
- [21] W. Lu, L. Xu, T. Yin, and L. Zhang. A highly accurate perfectly-matched-layer boundary integral equation solver for acoustic layered-medium problems. *SIAM Journal on Scientific Computing*, 45(4):B523–B543, 2023.
- [22] A. Meier and S. N. Chandler-Wilde. On the stability and convergence of the finite section method for integral equation formulations of rough surface scattering. *Mathematical Methods in the Applied Sciences*, 24(4):209–232, 2001.
- [23] D. Miret, G. Soriano, and M. Saillard. Rigorous simulations of microwave scattering from finite conductivity two-dimensional sea surfaces at low grazing angles. *IEEE Transactions on Geoscience and Remote Sensing*, 52(6):3150–3158, 2013.

- [24] P. Monk. *Finite element methods for Maxwell's equations*. Oxford university press, 2003.
- [25] F. Olver, D. Lozier, R. Boisvert, and C. Clark. Nist handbook of mathematical functions. *US Department of Commerce, National Institute of Standards and Technology*, 2010.
- [26] M. O’Neil and A. J. Cerfon. An integral equation-based numerical solver for taylor states in toroidal geometries. *Journal of Computational Physics*, 359:263–282, 2018.
- [27] M. Paulus, P. Gay-Balmaz, and O. J. Martin. Accurate and efficient computation of the green’s tensor for stratified media. *Physical Review E*, 62(4):5797, 2000.
- [28] C. Pérez-Arancibia and O. P. Bruno. High-order integral equation methods for problems of scattering by bumps and cavities on half-planes. *JOSA A*, 31(8):1738–1746, 2014.
- [29] M. Saillard and G. Soriano. Rough surface scattering at low-grazing incidence: A dedicated model. *Radio Science*, 46(05):1–8, 2011.
- [30] A. Sommerfeld. Über die ausbreitung der wellen inder drahtlosen telegraphie. *Annalen der Physik*, 333:665–736, 1909.
- [31] P. Spiga, G. Soriano, and M. Saillard. Scattering of electromagnetic waves from rough surfaces: A boundary integral method for low-grazing angles. *IEEE Transactions on Antennas and Propagation*, 56(7):2043–2050, 2008.
- [32] H. Wang and W. Lu. A high-accuracy mode solver for acoustic scattering by a periodic array of axially symmetric obstacles. *Journal of Scientific Computing*, 101(1):23, 2024.
- [33] X. Yu, G. Hu, W. Lu, and A. Rathsfeld. Pml and high-accuracy boundary integral equation solver for wave scattering by a locally defected periodic surface. *SIAM Journal on Numerical Analysis*, 60(5):2592–2625, 2022.
- [34] L. Zhang, L. Xu, and T. Yin. An accurate hypersingular boundary integral equation method for dynamic poroelasticity in two dimensions. *SIAM Journal on Scientific Computing*, 43(3):B784–B810, 2021.
- [35] Z. Zhao, L. Li, J. Smith, and L. Carin. Analysis of scattering from very large three-dimensional rough surfaces using mlfmm and ray-based analyses. *IEEE Antennas and Propagation Magazine*, 47(3):20–30, 2005.